

Computational Polarization 3D: new solution for monocular 3D imaging approach in natural conditions

Fei Liu (✉ feiliu@xidian.edu.cn)

Xidian University

Yudong Cai

Xidian University

Pingli Han

Xidian University

Xuan Li

Xidian University

Rongguang Liang

University of Arizona

Mingyu Yan

Xidian University

Xiaopeng Shao

Xidian University

Article

Keywords: monocular 3D polarization imaging, polarimetric properties, illumination

Posted Date: February 9th, 2021

DOI: <https://doi.org/10.21203/rs.3.rs-183031/v1>

License:   This work is licensed under a Creative Commons Attribution 4.0 International License.

[Read Full License](#)

Computational Polarization 3D: new solution for monocular 3D imaging approach in natural conditions

Fei Liu^{1,3,†}, Yu-dong Cai^{1,†}, Ping-li Han^{1,3,4,†}, Xuan Li¹, Rong-guang Liang², Ming-yu Yan¹, & Xiao-peng Shao^{1,3},

¹School of Physics and Optoelectronic Engineering, Xidian University, Xi'an 710071, China.

²James C. Wyant College of Optical Sciences, University of Arizona, Tucson, Arizona 85721, USA.

³Xi'an Key Laboratory of Computational Imaging, Xi'an 710071, China.

⁴the State Key Laboratory of Optical Engineering, Chinese Academic of Sciences, Chengdu 610209, China. †

Corresponding Author: xpshao@xidian.edu.cn; rliang@optics.arizona.edu

ABSTRACT

Analyzing the polarimetric properties of the reflected light is a simple, fast, and low-cost approach to recover shape information, but no reported method can accurately recover surface shape from non-Lambertian object in natural conditions with a single view. Another major issue is the lack of effective method to address azimuth ambiguity during the surface reconstruction. To address these two major obstacles, we propose a monocular 3D polarization imaging approach for non-Lambertian surfaces by investigating the subtle difference in specular and diffuse reflection and then separating them using independent component analysis (ICA). Separated pure diffuse reflection enables accurate polarization extraction, based on which a gradient field is derived to determine surface normals. The ambiguity is removed by solving an optimization problem with a reference gradient field. We experimentally demonstrate the performance of the proposed method with man-made object under the controlled illumination and human face under natural illumination.

INTRODUCTION

Shape information is essential in 3D computer vision with numerous applications ranging from unlocking a phone to city modeling¹⁻³. Various methods, including time of flight (ToF), structured light illumination, binocular stereo imaging, and Laser radar (LIDAR), have been developed⁴⁻⁸. However, all those methods are fairly complicated as special illumination or more than one view are always required. Shape information can also be estimated from polarization properties of the reflected light since that the shape of an object changes the polarization states of the reflected light⁹. The method of reconstructing the shape from polarization avoids some major drawbacks in other methods, such as active patterned illumination, multi viewpoints, high-speed detector (up to 1 ns), etc. The system for shape from polarization will be much simpler and lower cost, benefiting more applications including face recognition in security monitoring, outdoor experiments, and so on.

Approaches to extract shape from polarization rely on specular or diffuse reflections from an object. Methods based on specular polarization can often be restricted to conditions where specific lighting is used to ensure global specular reflection. Ikeuchi et al¹⁰

designed a spherical diffuser with a hole for the camera, several light sources outside the diffuser enabled light impinging from all directions to get specular reflection. However, specular reflection's uneven distribution will lead to non-unique normal direction, efforts have also been made to recover shape from diffuse polarization. Drbohlav and Sara¹¹ reconstructed shape from diffuse polarization over a single opaque sphere, but this method can't work to most natural objects. Atkinson and Hancock modified the physical model of shape from polarization to account for the cases where all the light is diffusely reflected^{12,13}. The degree and phase of diffuse polarization were used to estimate the zenith and the surface normal, respectively. To address the inevitable azimuth ambiguity, zenith angle was ranked for disambiguation¹². They tested the model over a variety of materials and explored the extent to which surface orientation can be estimated from diffuse polarization. They also used diffuse polarization in conjunction with shading from two views for shape estimation¹⁴. The surface normals were calculated from diffuse polarization for each view independently. Mahmoud et. al made efforts to recover shape from complete diffuse polarization from one view and one spectral imaging band¹⁵. They combined

shading and polarization to estimate surface normal and disambiguate the azimuth angle.

However, the reflected light from many objects is a combination of diffuse and specular reflection components¹⁶. As Atkinson et al denoted, a “mixed reflection” occurs: both diffuse and specular reflected light reach the detector¹². Many solutions often assume the object surface is Lambertian or complete specularity^{14,15,17-19}. But most real-world objects are complex in reflectance that violates the Lambertian assumption. A method that jointly used viewpoint and polarization was developed by Atkinson and Hancock to handle mixed reflection¹⁴, but a minimum of two viewpoints were required. Miyazaki et al. handled non-Lambertian surfaces by using an algorithm proposed by Tan and Ikeuchi^{20,21} to separate diffuse and specular reflection first, but the method excluded specular reflected light, resulting in errors over the specular reflection area. Another intrinsic drawback of using shape from polarization is the ambiguous estimation of surface orientation. Previous developed solutions to disambiguate the surface normal often assume convexity on surface or require assistance from extra views or multi-wavelength^{17,22-24}. Smith et. al²⁵ proposed an approach to estimate shape from a monocular polarization image and achieved favorable results, but this method didn't process reflection-mixed conditions as in non-Lambertian objects.

In this work, we present a monocular 3D imaging method using polarization properties of the reflected light from non-Lambertian objects in natural conditions. It first addressed the major obstacle of mixed reflection on non-Lambertian surfaces by first seeking the subtle difference in polarization between specular and diffuse reflection and then separating them using Independent Component Analysis (ICA), with neither prior information about the objects nor assistance from extra views. The separated pure diffuse reflection enables accurate polarization extraction, from which a gradient field is derived to determine surface normals. The ambiguity is addressed by solving an optimization problem with a reference gradient field. The key advantage of the proposed method is that it has the potential of recovering the shape of the non-Lambertian surface accurately with a single view. Detailed methods will be introduced in results.

RESULTS

Detection principles.

Theoretically, we can recover shape from the normal field determined by the zenith (θ) and azimuth (ϕ) angles, which can be derived utilizing Degree of Polarization (DoP) and Angle of Polarization (AoP) of the purely diffusely reflected light according to the Fresnel reflectance model as shown in Eq. (1)²⁶. The challenge is that the reflection on natural surfaces is neither completely diffuse nor specular. The region with specular reflection is often much brighter than other regions. According to Wolff's theory²⁷, light reflected from a surface arises from four different phenomena as illustrated by Fig. 1. Specular reflection is phenomenon 1. Reflection due to phenomena 2-3 are considered to be diffuse reflection, where phenomenon 3 makes major contribution to the diffuse reflection. Diffraction is phenomena 4 and is negligible. Most surfaces are non-Lambertian with both specular and diffuse reflection.

$$\begin{cases} DoP = \frac{(n-1/n)^2 \sin^2 \theta}{2 + 2n^2 - (n+1/n)^2 \sin^2 \theta + 4 \cos \theta \sqrt{n^2 - \sin^2 \theta}} \\ AoP = \frac{1}{2} \arctan \left(\frac{I_0 + I_{90} - 2I_{45}}{I_{90} - I_0} \right) = \phi - 90^\circ \text{ if } (I_{90} < I_0) \\ \left[\text{if } (I_{45} < I_0) \phi = AoP + 180^\circ \text{ else } \phi = AoP \right] \end{cases} \quad (1)$$

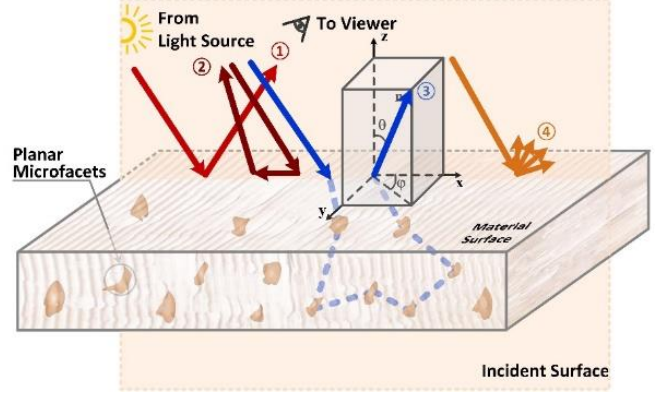


Fig. 1 Reflection of light from a material surface ① specular reflection; ② - ③ diffuse reflection; and ④ diffraction. Most objects reflect light in both specular and diffuse patterns at the same time.

In polarization detection, polarization information can be obtained with a camera and a rotated linear polarizer mounted in front of it or a camera with a pixelated polarizer²⁸. DoP is interpreted based upon the observed maximum and minimum pixel brightness I_{max} and I_{min} during polarizer rotation²⁹. Since reflection from most surfaces is a combination of specular and diffuse reflection, the detected polarization images I_{max} and I_{min} can be expressed as $I = f_b \cdot I^{sub}$ ($sub = spec \text{ or } diff$), where the superscripts $spec$ and $diff$ indicate specular and diffuse reflection, respectively, and coefficient f_b balances the difference in intensity between the specular and diffuse reflection. Thus, DoP should follow the detailed expression in Eq. (2),

$$\begin{aligned} DoP &= \frac{f_b (I_{max}^{spec} - I_{min}^{spec}) + (I_{max}^{diff} - I_{min}^{diff})}{f_b (I_{max}^{spec} + I_{min}^{spec}) + (I_{max}^{diff} + I_{min}^{diff})} \\ &\propto \{ DoP^{spec}, DoP^{diff} \} \end{aligned} \quad (2)$$

Typically, DoP is used to recover shape. However, accurate shape recovery of non-Lambertian objects requires DoP^{diff} , which measures polarization information from completely diffuse reflection since it's not sensitive to light incidence direction and distributes more equally on the whole surface than specular reflection.

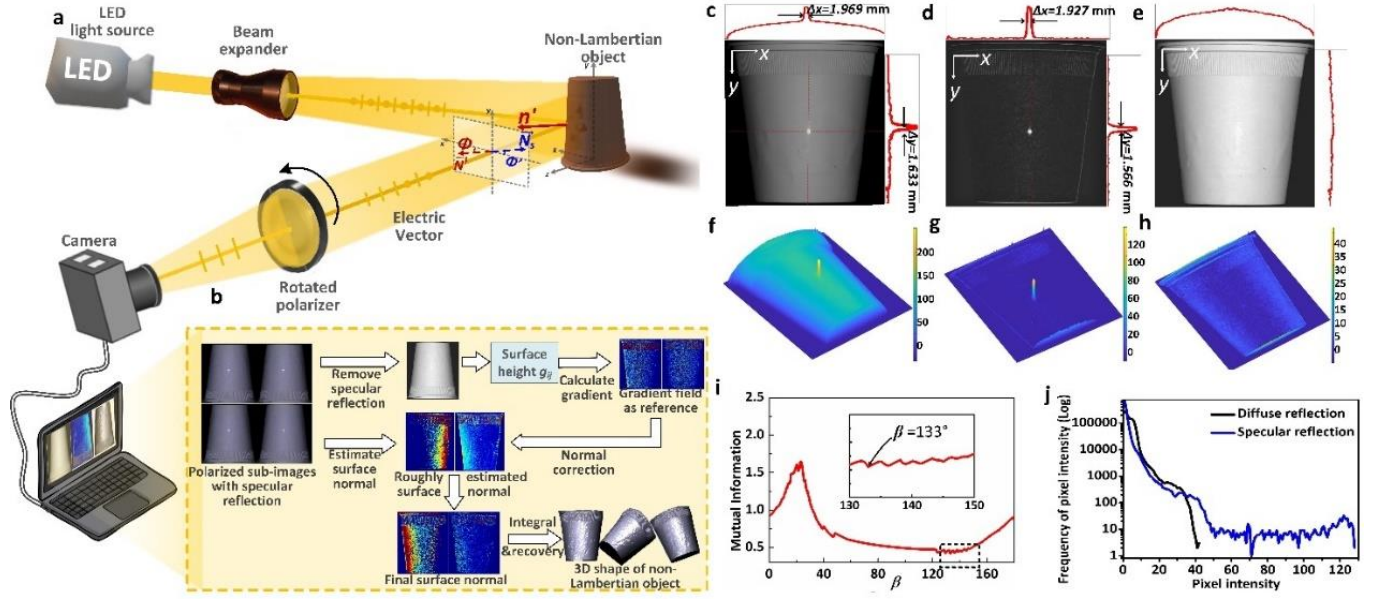


Fig. 2. Overall schematic workflow. a) Polarization detection process. The light source provides unpolarized illumination in indoor experiments, and it's not necessary in outdoor conditions. Polarization information from the reflected light can be obtained with a camera and a rotated linear polarizer mounted in front of it or a camera with a pixelated polarizer. b) Mixed reflection separation and 3D information interpretation. c) raw intensity image of a foam cup with diffuse and specular reflection. d) separated specular reflection. e) Separated diffuse reflection. f, g) and h) 3D display of intensity image of c), d) and e). i) Mutual information of the estimated diffuse and specular reflection. The coefficient β can be determined by locating the lowest value to enable diffuse and specular reflection separation described in "Methods". j) The frequency of the pixel intensity of diffuse and specular reflection. Only specular reflection reaches intensity over 40, corresponding to the bright area in Fig.2(c). Both specular and diffuse reflection distribute mainly over range below 40, demonstrating that the surface is generally covered by mixed reflection.

Separation of specular and diffuse reflection.

Figure 2a shows schematically the proposed method. The imaging system consists of an ordinary LED light source to provide unpolarized illumination in indoor environment and a rotated polarizer mounted in front of a camera to capture polarized sub-images. Figure 2b details the post-processing method. Figure 2c-2h illustrate one example with mixed reflection. Specifically, the object is a foam cup with rough surface under illumination of unpolarized light from a Thorlabs MNWHL4 LED light source. The prominent specular reflection area is about $1.96 \text{ mm} \times 1.63 \text{ mm}$, whose shape cannot be estimated accurately from the polarization information with mixed reflection (Fig. 2c). Therefore, it is necessary to separate the specular reflection from the mixed reflection. This is very challenge, particularly without prior information. In this paper, we introduce an effective method to accurately extract the specular reflection from the mixed reflection. Stemming from the Fresnel reflection model^{26,30}, the diffuse and specular reflection components are partially polarized as well. The observed intensity could be taken as a combination of completely polarized light and unpolarized light. According to Stokes theory³¹, polarization imaging usually requires four images with a polarizer oriented at $0^\circ, 45^\circ, 90^\circ$ and 135° relative to a chosen reference orientation. Then the observed image can be taken as a combination of completely polarized light and unpolarized light as shown by Eq. (3),

$$I_i = f_d(\delta_i) \mathcal{I}_p^{\text{diff}} + f_s(\delta_i) \mathcal{I}_p^{\text{spec}} + \mathcal{I}_{np}^0, i = 0^\circ, 45^\circ, 90^\circ, 135^\circ \quad (3)$$

where $\mathcal{I}_p^{\text{diff}}$ and $\mathcal{I}_p^{\text{spec}}$ are the pure polarized components in diffuse and specular reflection, respectively, and \mathcal{I}_{np}^0 is the unpolarized

component. The coefficients $f_d(\delta_i)$ and $f_s(\delta_i)$ are functions of the orientation δ_i of the polarizer. I_i is partially linearly polarized since natural light or reflected light by surfaces contains very little circular polarization components which can be ignored. The unpolarized components \mathcal{I}_{np}^0 can then be related to I_{\min} ($\mathcal{I}_{np}^0 = 2I_{\min}$) which can be calculated by Stokes Vector. Taken the incoherence between each frame into consideration, it's possible to build a linear independent function based on I_i and I_{\min} , as shown in Eq. (4),

$$I_D = I_i - I_{\min} = M \cdot S$$

$$= [f_d(\delta_i) \quad f_s(\delta_i)] \cdot \begin{bmatrix} \mathcal{I}_p^{\text{diff}} \\ \mathcal{I}_p^{\text{spec}} \end{bmatrix} = \begin{bmatrix} 1 & f_s(\delta_0) \\ 1/2 & f_s(\delta_{45}) \\ 0 & f_s(\delta_{90}) \\ 1/2 & f_s(\delta_{135}) \end{bmatrix} \cdot \begin{bmatrix} \mathcal{I}_p^{\text{diff}} \\ \mathcal{I}_p^{\text{spec}} \end{bmatrix} \quad (4)$$

where I_D is the difference between two frames, and M indicates the modulation of the polarizer to light intensity. For simplicity, we take the orientation at which the polarization orientation of diffuse reflection coincides with the orientation of the polarizer as 0° , namely $I_0 = I_{\max}$. Therefore, the modulation to diffuse reflection follows $f_d(\delta_i) = f_d(\delta_0) \cos^2 \delta_i$, $\delta_0 = 0^\circ$ with polarizer orientated at angle δ_i during rotation. As the polarized diffuse and specular reflection differ in orientation, the modulation function of specular reflection will keep its original formation.

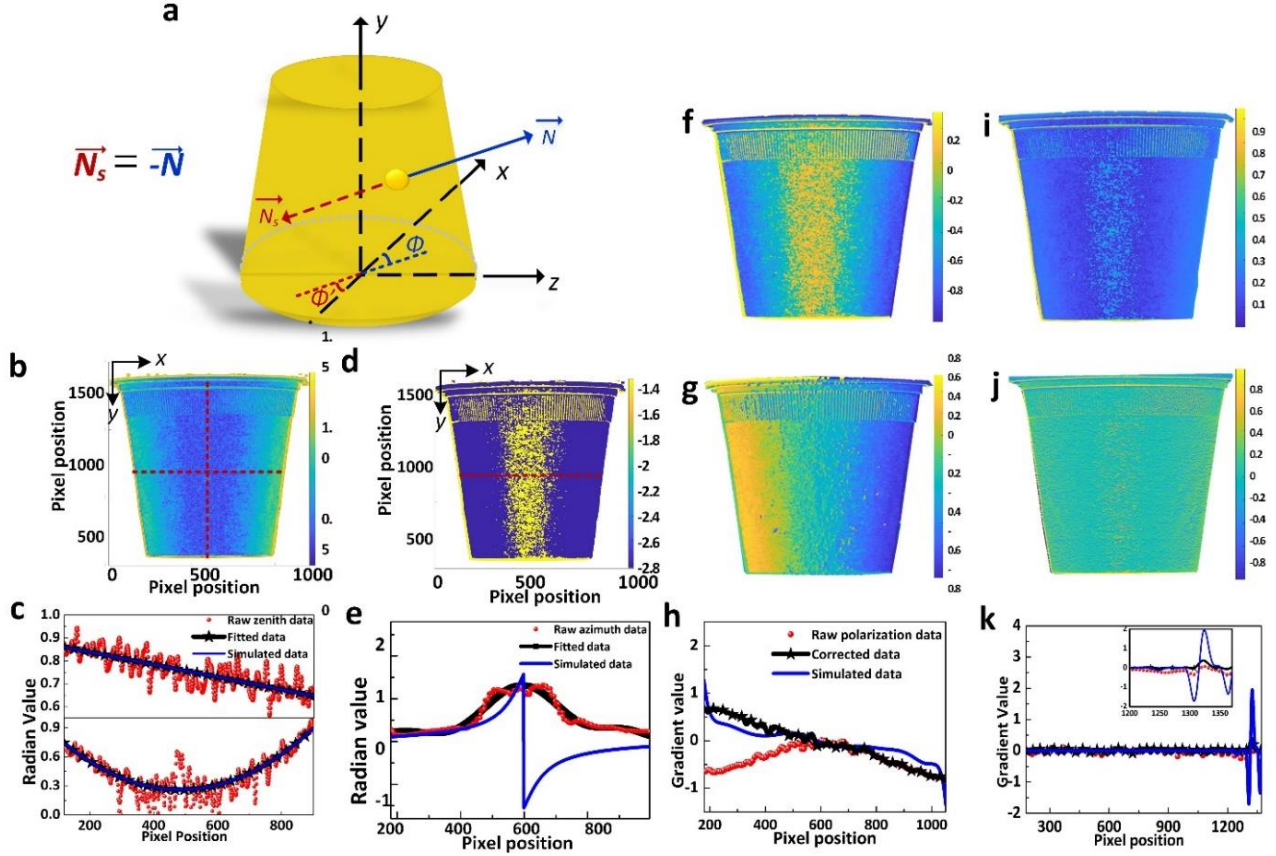


Fig. 3 Surface normal correction. a) Display of surface normal ambiguity. For one point, $\tan \phi = \tan \phi'$, the estimated normal can be \vec{N} or $-\vec{N}$, which are in opposite directions. b) and d) raw zenith and azimuth data derived from polarization. c) raw and fitted zenith in comparison with the ideal simulated data where inversion occurs around pixel 600. f) $G^{polar}\{grad(x)\}$, g) $G^{cor}\{grad(x)\}$, i) $G^{polar}\{grad(y)\}$; j) $G^{cor}\{grad(y)\}$. h) Intensity variations of pixels in Row 700 of f) and g) in comparison with the simulated data, data before 600 requires correction in x direction. k) intensity variations of pixels in Column 650 of i) and j) in comparison with the simulated data, no correction is required in y direction.

To separate diffuse and specular reflection, we need to decompose the given observation matrix I_D into a product of two matrices, M and S , stemming from ICA theory^{32,33}. Hence, we build the optimization algorithm in order to determine the accurate matrix M and S (Methods section). The diffuse and specular reflection components f_p^{diff} and f_p^{spec} can then be separated by use of Mutual Information (MI)^{34,35}. The separated specular and diffuse reflection components from Fig. 2c are shown in Figs. 2d and 2e, respectively. The specularly reflected light can be accurately located and separated, the region with strong specular reflection is about 1.92mm * 1.52mm, slightly smaller than the dimension (1.96mm * 1.63 mm) estimated from the intensity image. Besides, Figs. 2d and 2g indicate that the specular reflection occurs almost everywhere on the cup surface, but with the strongest reflection around the center of the cup surface. Figures 2e and 2h demonstrate that the diffuse reflection is relatively uniform over the cup surface. It's ideal for shape recovery as the normal field can be accurately estimated from the diffuse reflection for 3D shape imaging. Besides, Figure 2j shows intensity frequency of specular and diffuse reflection, indicating that specular reflection happens at almost every point. Although the captured image shows only one obvious bright area, it's necessary to identify and remove it from the entire surface.

Surface normal correction.

To recover the shape of an object with $n \times n$ pixels after separating specular and diffuse reflection from the captured image, we need to accurately determine $2n^2$ unknowns (θ, ϕ) . Based on accurate (θ, ϕ) , gradient field G^{polar} is first calculated and the shape can be recovered (Method section). According to the polarization information from the separated diffuse reflection, we can get $2n^2$ Eq. (1), based on which accurate (θ, ϕ) can be theoretically calculated. However, the arctangent function in Eq. (1) results in multi-valued ϕ , i.e., the azimuth ambiguity, which is the major problem in shape from polarization. Figure 3a illustrates how surface normal ambiguity generates. According to the monotonicity of Eq. (1), we can directly calculate zenith as shown in Fig. 3b. Figure 3c illustrates data variation of Column 890 in vertical direction and Row 651 in horizontal direction. The raw zenith data show the traceable trend in spite of fluctuation resulting from noise. After fitting, θ keeps in the expected range between 0 to $\pi/2$, and presents an ideal variation along with the shape, demonstrating that accurate zenith is achievable from diffuse polarization. Unfortunately, the essential problem that fails shape recovery is the azimuth ambiguity. It results in mistakes in estimating surface normal and further deforms the recovered 3D information.

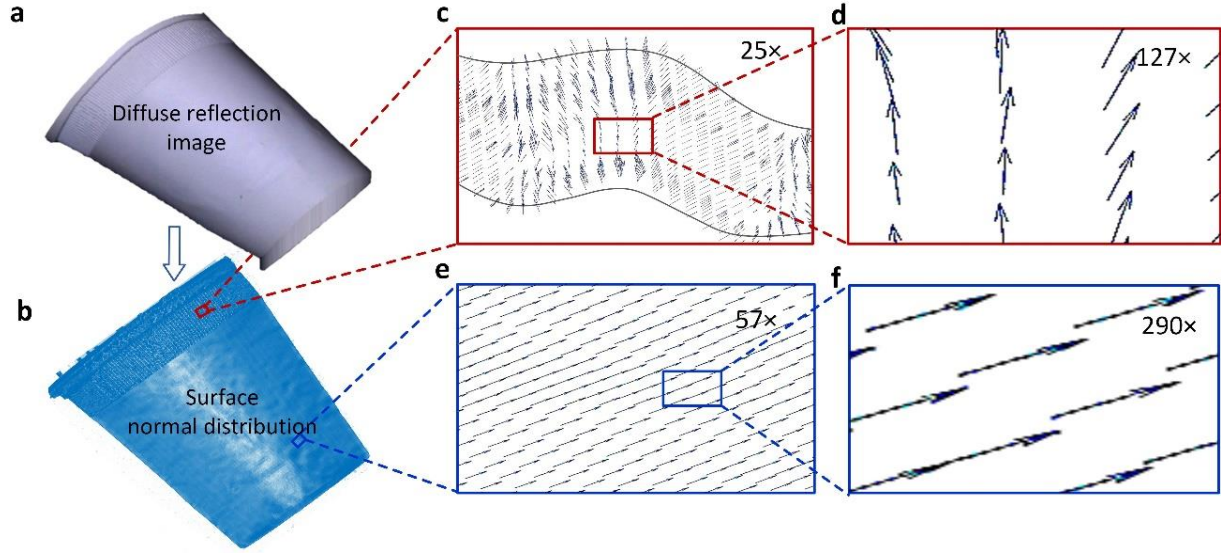


Fig. 4 Normal field after correction. a) Overall surface normal display, b) and c) 25 times and 127 times magnification of the normals in the region with grooves, d) and e) 25 times and 127 times magnification of the normals in the body. The subtle difference in the directions of the normals are clearly indicated in c) and d), which is crucial to recover the accurate shape.

Taken as an example in Fig. 3a, azimuth angle ϕ and ϕ' have same projection value, but two different surface normals \hat{N} and \hat{N}_s are in opposite directions due to the arctangent function. Only one of these two normals is correct. Figure 3d illustrates the azimuth information estimated from AOP. Data in Row 651 is plotted in Fig. 3e, where the ambiguity problem is clearly indicated. The azimuth variation doesn't follow the shape fluctuation from pixel 600. We can't determine the final accurate normal by only AOP information.

Fortunately, though the azimuth is ambiguous, the relative height of surface has been accurately determined from the separated diffuse reflection. To determine the unique accurate normal, we only require an additional constraint to azimuth, i.e., normal direction. Lambertian reflectance model describes diffuse reflection over surface shape³⁶. Under total Lambertian reflection, stronger intensity in an image means closer distance between an object and the detector, which relates surface shape to image intensity. Here we employ the Lambertian reflection model³⁷ to convert captured intensity data into height data and then obtain the gradient field G^{depth} (Models section). It's used as a reference gradient field to correct the perturbed gradient field G^{polar} derived from polarization by an optimization function in Eq. (5),

$$\hat{A} = \arg \min_A \left\| G^{depth} - A(G^{polar}) \right\|_2^2, \quad A \in \{1, -1\} \quad (5)$$

where \hat{A} is a set of binary operands and A is a binary operator. If $A=1$, it means the estimated azimuth is accurate; and if $A = -1$, removing ambiguity is required by changing the direction of

estimated surface normal by changing ϕ into $\phi + \pi$. The correction is implemented by $G^{cor} = \hat{A} \cdot G^{polar}$. Till now, with the constraint from G^{depth} to direction of G^{polar} , the azimuth ambiguity is addressed. And final accurate surface normal can then be determined by Eq. (5) as we discussed.

As a demonstration, Figs. 3f and 3i present the directly calculated gradient field components $G^{polar}\{grad(x)\}$ and $G^{polar}\{grad(y)\}$, while Figs. 3g and 3j are $G^{cor}\{grad(x)\}$ and $G^{cor}\{grad(y)\}$ after correction, respectively. The difference in intensity distribution presents how correction amends the gradient field. Figure 3h plots the intensity variations of the horizontal red dotted lines in Fig. 3f and 3g versus the horizontal pixel position. $G^{cor}\{grad(x)\}$ progressively decreases along with the surface in x direction, which is reasonable considering its geometry shape. However, $G^{polar}\{grad(x)\}$ from the raw polarization data increases first and then decreases after Pixel 600. In comparison, the corrected data display a much higher level of compliance with the gradient variation along with the cup's surface as shown by the ideal simulated data, indicating that the accurate shape can be achieved from the corrected data. Similarly, $G^{polar}\{grad(y)\}$ from Fig. 3i and $G^{cor}\{grad(y)\}$ from Fig. 3j along the vertical red dotted line also prove good coupling with surface variation in y direction which is a straight line with a constant gradient except the rim of the cup. This example demonstrates that the proposed method can solve the problem of surface normal ambiguity, ensuring accurate shape recovery.

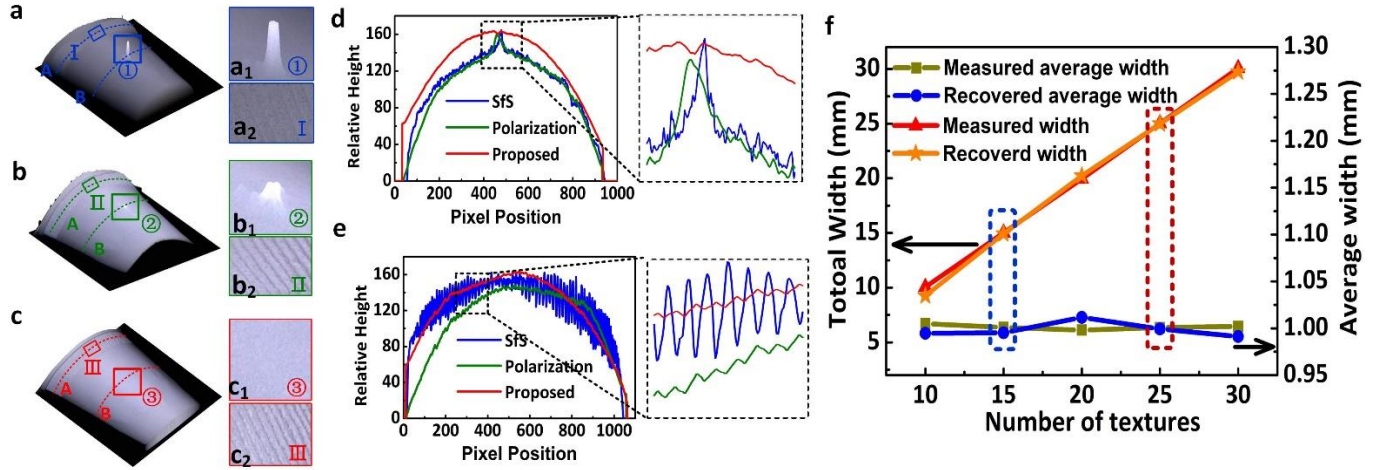


Fig. 5 Recovered surface shape of the foam cup. a) Shape from shading. b) traditional shape from polarization, and c) the proposed method. Zoom-ins of the ROIs ①, ② and ③ are shown in a₁, b₁ and c₁, I, II and III are shown in a₂, b₂ and c₂. d) contours of line A and e) contours of line B compare the performance of three different methods. f) accuracy comparison between the recovered and measured surface groove.

Application to man-made Non-Lambertian surface.

We experimentally demonstrated the developed method for shape recovery of non-Lambertian objects with mixed specular and diffuse reflection by first imaging a man-made object, a textured foam cup, for validation under controlled unpolarized illumination as shown in Fig. 2a. Figure 4b plots the finally estimated surface normal distribution from the separated diffuse reflection from Fig. 4a (details see Supplementary video 1). Figure 4c is a 25x zoomed view of a small region with the grooves on the cup surface. Many surface normals in unit length can be observed, whose distribution varies with the grooves. The 127 zoomed view in Fig. 4d further shows the subtle variation. In contrast, the normals from the body part in Figs. 4e and 4f are in a pretty unanimous direction.

The target surface was overall rough but locally smooth. Therefore, noticeable specular reflection components can be seen from the captured images. Two typical monocular 3D imaging methods, Sfs and SfP, were also tested for qualitative comparison. Figure 5a is the shape from Sfs where the region with strong specular reflection was constructed as a big bump as shown in Fig. 5a1. This is due to the limitation in Sfs that the stronger intensity corresponds to closer distance between the object to the camera. The results in Figs. 5b and 5b1 from SfP also show that the region with strong specular reflection was reconstructed incorrectly with a small bump. In comparison, the proposed method can recover the regions with strong specular reflection accurately. As shown in Fig. 5c1 the smooth surface was reconstructed without any unexpected bumps. The profile lines along the dotted line B in Figs. 5e clearly demonstrate the significant improvement of the proposed method. Figures 5a2, 5b2, 5c2 and 5d further compare the shape reconstructions of the regions with grooves. The grooves with a feature depth of 0.3mm could be recovered more accurately by the proposed method than SfP,

but Sfs failed completely where the grooves were constructed in the opposite direction.

We measured 10, 15, 20, 25, and 30 grooves to estimate the groove width with a digital caliper. The averaged width was 1.00mm. Figure 5f compares the measured and reconstructed total width and averaged width where only subtle error to 0.1mm occurs, demonstrating the accuracy of the recovered surface shape.

Application to real human face in natural condition.

To further demonstrate the performance of the proposed method, we imaged a human face under natural illumination in outdoor. Unlike the man-made target, human face is much more complex in structure and details. Natural illumination is more complex with uncontrolled direction, intensity, and polarization. Figure 6a illustrates the experiment condition and setup.

Figures 6b and 6c are the color image and intensity distribution of the human face. Figures 6d and 6e are the zoomed-in region and its intensity distribution. Strongly uneven intensity distribution and inevitable mixed reflection were two obstacles for face reconstruction. Either problem failed SfS reconstruction as shown by Figs. 6f and 6i where almost all the face features were lost. Figures 6g is three different views of the reconstructed human face by the proposed method, as detailed in Supplementary video 2. The features visualized in the 3D renderings fit well with their original appearance, and some fine features can be easily identified. Figure 6h plots the vertical and horizontal face profiles along the red and black lines in Figs. 6g. The results demonstrated neither mixed reflection nor uneven illumination prevented the proposed method from reconstructing surface shape accurately due to its capability of separating mixed reflection and estimating accurate diffuse reflection. From the proposed method we can get the surface normals pixel by pixel, and further the whole 3D rendering of the face. The point cloud data in Fig. 6j and 6k demonstrate the well-recovered face features and good resolution.

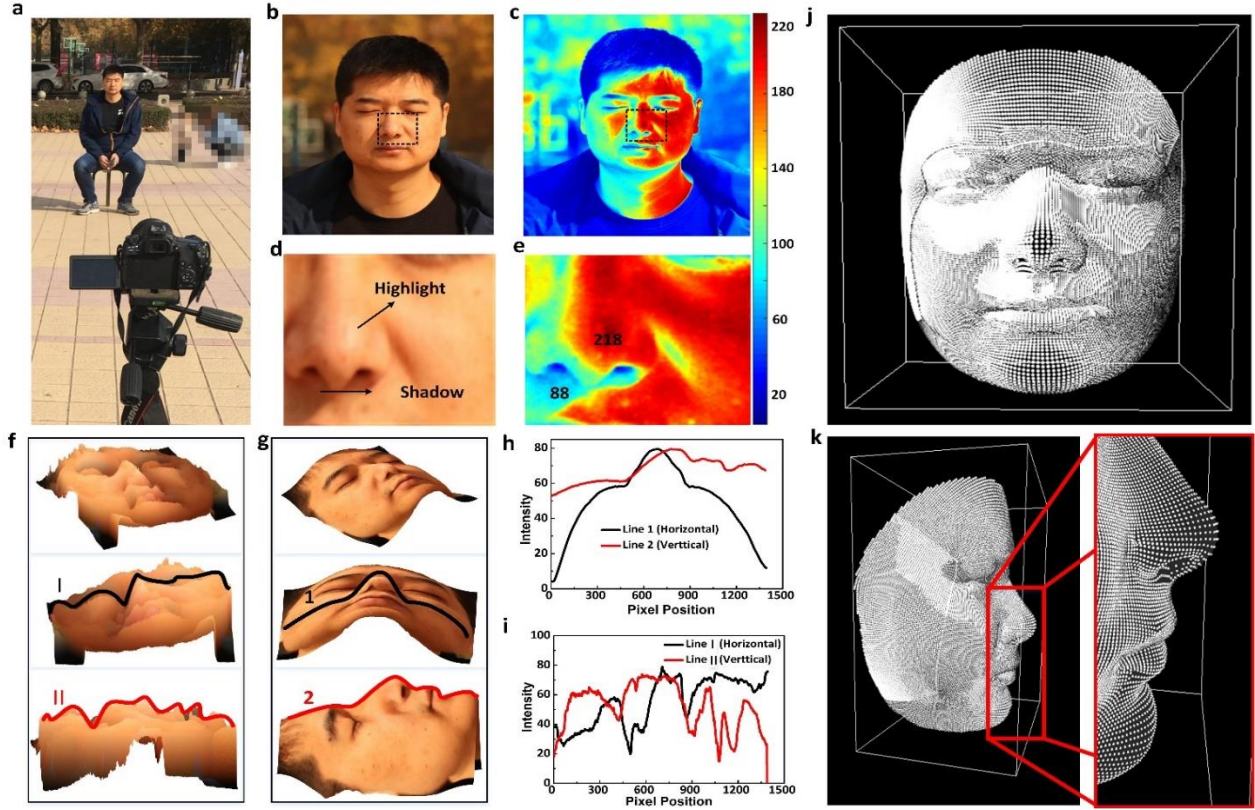


Fig. 6 3D imaging of human-face in natural conditions. a) Experiment setup and condition. b) captured human face, and c) intensity distribution. d) and e) zoomed-in highlighted area and intensity distribution. f) and g) three different views of recovered 3D human face by shape from shading and proposed method. h) and i) two contours of recovered face from f) and g). j) and k) cloud data of the recovered human face by the proposed method.

DISCUSSION

we have introduced a monocular shape recovery method based on polarization information with a single view even for non-Lambertian surfaces in natural conditions. Classical shape from polarization methods strongly depend on reflection conditions, either pure specular or diffuse reflection. It is almost impossible in natural environments since non-Lambertian surfaces dominate the real world, leading to mixed reflection and further deforming recovered shape. The method is featured by two major contributions: mixed reflection separation and azimuth deambiguity. By making use of the subtle difference in polarization between diffuse and specular reflection, it can accurately locate and remove specular components and estimate accurate diffuse components, making it possible to

METHODS

Experiment setup.

In application to man-made non-Lambertian target, a textured foam cup was located 2m away from the imager LUCID TRI050S-P, by which the four polarized images were captured. A Thorlabs MNWHL4 LED light source was used to provide unpolarized illumination. The four polarized images were the only raw data we used in this study to recover surface. In application to real human-face in natural condition, a Thorlabs WP50L-UB polarizer was mounted in front of the Canon E77D with 4000×6000 pixels to capture four polarization images by manually rotating it. The images were captured at about 11:00 am in early winter when the human subject faced south at a 5m distance from the camera. Sunlight directly illuminated the left face.

Optimization model.

recover shape of non-Lambertian surfaces. It estimates pixel-to-pixel normal gradient field, which solves the problem in shape from polarization that normal azimuth is in ambiguity by providing a correcting reference. Classical methods always require assistance from multi-views, multi-wavelength or extra device. Moreover, the proposed method can achieve micron-level depth resolution which is validated in experiment with controlled illumination and outdoor environment under natural illumination. With the excellent accuracy and ability to recover shape by a single view, the proposed method has the great potential in the fields of biomedicine, archaeology, secure payment, and so on. Future work would be to explore the approaches to recover shape information of a whole continuous scene, for instance, crowded customers in shopping mall or running vehicles on road.

For $f_d(\phi_0)I_p^{diff}$, $f_d(\phi_0)$ is a determined coefficient, which only changes the brightness of the image. Since the rank of matrix M and S is 2, the rank of $M \cdot S$ should also be 2. Here we approximate I_D by a matrix of rank 2 using the Singular Value Decomposition (SVD). I_D can be represented as $I_D = UDV^T$, where U and V are orthogonal matrix, D is the singular value matrix of I_D . To keep matched dimensions between decomposed and desired matrices, a 2×2 nonsingular orthogonal matrix W is introduced in Eq. (6).

$$I_D = \underset{M}{U} \underset{S}{W}^{-1} \underset{S}{D} \underset{M}{V}^T \quad (6)$$

Matrices M and S are both expressed by W . Given that W is nonsingular and orthogonal, it's reasonable to assume it has the formation $W = (r_1 \cos \alpha \ r_2 \cos \beta, \ r_1 \sin \alpha \ r_2 \sin \beta)$, where r_1 and r_2 are two positive numbers. Equation (4) indicates the first column of M is a constant vector. Here we build the optimization

function in Eq. (7) in order to make the first column vector as close to the constant vector as possible.

$$J_1 = \arg \min_{r_1, \alpha} \left\| U \begin{bmatrix} r_1 \cos \alpha \\ r_1 \sin \alpha \end{bmatrix} - \begin{bmatrix} 1 \\ 1/2 \\ 0 \\ 1/2 \end{bmatrix} \right\|^2 \quad (7)$$

Since column vectors of U are orthogonal, the minimization problem is solvable, i.e., r_1 and α can be determined. For r_2 and β , we start from the determinant Δ of W $\det(W) = \Delta = r_1 r_2 \sin(\beta - \alpha)$, whose absolute value corresponds to the intensity of the specular reflection image. Aiming to separate specular reflection, we can set $|\Delta|=1$ without losing generality. With known r_1 and α , if either r_2 or β is determined, the other one is determined as well. For this purpose, we gradually change β within range $[0, \pi]$, each (β, r_2) corresponds to a pair of diffuse and specular reflection image. By comparing their mutual information (MI) indicated by Eq. (8), a quantity that measures mutual statistical dependency of the two random variables, we can separate diffuse and specular reflection by searching for the minimum value,

$$\text{MI}(\mathcal{I}_p^{\text{diff}}; \mathcal{I}_p^{\text{spec}}) = \sum_{i=1}^L \sum_{j=1}^L p(x_i, y_j) \log \frac{p(x_i, y_j)}{p(x_i)p(y_j)} \quad (8)$$

where $p(x_i)$ and $p(y_j)$ are the histograms of the diffuse and specular reflection images, $p(x_i, y_j)$ is their joint histogram, x_i and y_j are bins of the histograms. For the object in Fig. 2(a), $\mathcal{I}_p^{\text{diff}}$ and $\mathcal{I}_p^{\text{spec}}$ are dependent on MI as indicated by Eq. (8). And then r_2 can be determined using $|\Delta| = |r_1 r_2 \sin(\beta - \alpha)| = 1$. With (r_1, α) and (r_2, β) , diffuse and specular reflection can be separated.

Gradient field acquisition.

We calculate gradient field through surface normal azimuth and zenith angle, which is defined by

$$\begin{aligned} G^{\text{polar}} &= \{ \text{grad}^{\text{polar}}(x), \text{grad}^{\text{polar}}(y) \}, \\ \text{grad}^{\text{polar}}(x) &= \tan \theta \cos \phi \\ \text{grad}^{\text{polar}}(y) &= \tan \theta \sin \phi \\ Z(x, y) &= F^{-1} \left\{ -j \frac{\frac{2\pi u}{N} F\{\text{grad}(x)\} + \frac{2\pi v}{N} F\{\text{grad}(y)\}}{\left(\frac{2\pi u}{N}\right)^2 + \left(\frac{2\pi v}{N}\right)^2} \right\} \end{aligned} \quad (9)$$

where $F\{\cdot\}$ and $F^{-1}\{\cdot\}$ are Fourier transform and inverse Fourier transform, respectively.

Conversion model.

We employ the Lambertian reflection model to convert the intensity data into height data, and then obtained the gradient field data.

$$f(g_{m,n}^{\text{depth}}) = I_{m,n} - R(\text{grad}^{\text{depth}}(x), \text{grad}^{\text{depth}}(y)) = 0$$

$$\begin{cases} \text{grad}^{\text{depth}}(x) = \frac{\partial g_{m,n}^{\text{depth}}}{\partial x} = g_{m,n}^{\text{depth}} - g_{m,n-1}^{\text{depth}}; \\ \text{grad}^{\text{depth}}(y) = \frac{\partial g_{m,n}^{\text{depth}}}{\partial y} = g_{m,n}^{\text{depth}} - g_{m-1,n}^{\text{depth}} \end{cases} \quad (11)$$

where, $R(\cdot)$ means the reflectance function, $g_{m,n}^{\text{depth}}$ is the surface height, m and n indicate the pixel position in X and Y directions, respectively, and $G^{\text{depth}} = \{ \text{grad}^{\text{depth}}(x), \text{grad}^{\text{depth}}(y) \}$ is the gradient field derived from image intensity. For $f(g_{m,n}^{\text{depth}}) = 0$, by taking the first two orders of its Taylor expansion we can get the expression of gradient field in Eq. (12),

$$\text{grad}_{m,n}^{\text{depth}}(k) = \text{grad}_{m,n}^{\text{depth}}(k-1) - \left(\frac{f(\text{grad}_{m,n}^{\text{depth}}(k-1))}{\frac{\partial f}{\partial \text{grad}_{m,n}^{\text{depth}}}(\text{grad}_{m,n}^{\text{depth}}(k-1))} \right) \quad (12)$$

where $\text{grad}_{m,n}^{\text{depth}}(k-1)$ indicates the gradient field $\text{grad}_{m,n}^{\text{depth}}$ after $k-1$ iterations. Given an initial value $\text{grad}_{m,n}^{\text{depth}}(0)$, G^{depth} is then determined by Eq. (12), which can accurately locate direction of surface normal at each pixel.

DATA AVAILABILITY

The datasets generated and analyzed during this study are available from the corresponding author on reasonable request.

COLD AVAILABILITY

MATLAB codes for data processing, analysis, and algorithm implementation performed in this study are available from the corresponding author on reasonable request.

REFERENCES

1. B.-Q. Sun, M.-P. Edgar, R. Bowman, L.-E. Vittert, S. Welsh, A. Nowman, M.-J. Padgett, 3D computational imaging with single-pixel detectors. *Science* 340, 844-847 (2013).
2. R. Prevedel, Y.-G. Yoon, M. Hoffmann, N. Pak, G. Wetzstein, S. Kato, T. Schrodel, R. Raskar, M. Zimmer, E.-S. Boyden, A. Vaziri, Simultaneous whole-animal 3D imaging of neuronal activity using light-field microscopy. *Nat. Methods* 11, 727-730 (2014).
3. K. Morimoto, A. Ardelean, M.-L. Wu, A.-C. Ulku, I.-M. Antolovic, C. Nruschini, E. Charbon, Megapixel time-gated SPAD image sensor for 2D and 3D imaging application. *Optica* 7, 346-354 (2020).
4. F.-Q. Li, H.-J. Chen, A. Pediredla, C. Yeh, K. He, A. Veeraraghavan, O. Cossairt, CS-ToF: high-resolution compressive time-of-flight imaging. *Opt. Express* 25, 31096-31110 (2017).
5. M.-J. Sun, M.-P. Edgar, G.-M. Gibson, B.-Q. Sun, N. Radwell, R. Lamb, M.-J. Padgett, Single-pixel three-dimension imaging with time-based depth resolution. *Nat. Commun.* 7, 12010 (2016).
6. S. Heist, C. Zhang, K. Reichwald, P. Kühmstedt, G. Notni, A. Tünnermann, 5D hyperspectral imaging: fast and accurate measurement of surface shape and spectral characteristics using structured light. *Opt. Express* 18, 23366-23379 (2018).
7. D. Mo, R. Wang, N. Wang, T. Lv, K.-S. Zhang, and Y.-R. Wu, Three-dimensional inverse synthetic aperture lidar imaging for long-range spinning targets. *Opt. Lett.* 4, 839-842 (2018).
8. J.-H. Sun, Y. Zhang, X.-Q. Cheng, A high precision 3D reconstruction method for bend tube axis based on binocular stereo vision. *Opt. Express* 3, 2292-2304 (2019).
9. D. Miyazaki, R.-T. Tan, K. Hara, K. Ikeuchi, Polarization-based inverse rendering from a single view. In *proc. IEEE International Conference on Computer Vision (ICCV)* 2, 982-987 (Nice, France, 2003).
10. M. Saito, Y. Sato, K. Ikeuchi, H. Kashiwagi, Measurement of surface orientations of transparent objects by use of polarization in highlight. *J. Opt. Soc. Am. A* 9, 2286-2293 (1999).

11. O. Drbohlav, R. Sara, Using polarization to determine intrinsic surface properties. *Proc. SPIE* 3826, 253-263 (1999).
12. G.-A. Atkinson, E.-R. Hancock, Recovery of surface orientation from diffuse polarization. *IEEE Trans. Image Process* 15, 1653-1664 (2006).
13. S.-K. Nayar, X.-S. Fang, T. Boulton, Separation of reflection components using color and polarization. *Int. J. Comput. Vision* 21, 163-186 (1997).
14. G.-A. Atkinson, E.-R. Hancock, Shape estimation using polarization and shading from two views. *IEEE Trans. Pattern Anal. Mach. Intell.* 11, 2001-2017 (2007).
15. A.-H. Mahmoud, M.-T. El-melegy, A.-A. Farag, Direct method for shape recovery from polarization and shading. *Proc. IEEE International Conference on Image Processing* 13367820, 1769-1772 (Orlando, USA, 2012).
16. L.-B. Wolff, Relative brightness of specular and diffuse reflection. *Opt. Eng.* 33, 285-293 (1994).
17. A. Kadambi, V. Taamazyan, B. Shi, R. Raskar, Depth sensing using geometrically constrained polarization normal. *Int. J. Comput. Vision* 125, 34-51 (2017).
18. D. Miyazaki, M. Kagesawa, K. Ikeuchi, Transparent surface modeling from a pair of polarization images. *IEEE Trans. Pattern Anal. Mach. Intell.* 26, 73-82 (2004).
19. M. Oren, S.-K. Nayar, A theory of specular surface geometry. *Int. J. Comput. Vision* 24, 105-124 (1997).
20. Umeyama, S., & Godin, G. Separation of diffuse and specular components of surface reflection by use of polarization and statistical analysis of images. *IEEE Trans. Pattern Anal. Mach. Intell.* 26, 639-647 (2004).
21. R.-T. Tan, K. Ikeuchi, Separating reflection components of textured surfaces using a single image. In: *Digitally Archiving Cultural Objects*. (Springer, 2008).
22. C. Stolz, M. Ferraton, F. Meriaudeau, Shape from polarization: a method for solving zenithal angle ambiguity. *Opt. Lett.* 37, 4218-4220 (2012).
23. D. Miyazaki, T. Shigetomi, M. Baba, R. Furukawa, S. Hiura, N. Asada, Surface normal estimation of black specular objects from Multiview polarization images. *Opt. Eng.* 56, 041303 (2016).
24. S.-G. Park, J.-H. Kim, S.-W. Min, Polarization distributed depth map for depth-fused three-dimensional display. *Opt. Express* 5, 4316-4323 (2011).
25. R. Huang, W.-A.-P. Smith, Shape-from-shading under complex natural illumination. *Proc. IEEE International Conference on Image Processing*, 12504511, 13-16 (Brussels, Belgium, 2011).
26. H.-D. Tagare, R.-J.-P. deFigueiredo, A theory of photometric stereo for a class of diffuse non-lambertian surface. *IEEE Trans. Pattern Anal. Mach. Intell.* 13, 133-152 (1991).
27. L.-B. Wolff, T.-E. Boulton, Constraining object features using a polarization reflectance model. *IEEE Trans. Pattern Anal. Mach. Intell.* 13, 635-657 (1991).
28. X.-Z. Tu, O.-J. Spires, X.-B. Tian, N. Brock, R.-G. Liang, S. Pau, Division of amplitude RGB full-Stokes camera using micro-polarizer arrays. *Opt. Express* 26, 33160-33175 (2017).
29. F. Liu, P.-L. Han, Y. Wei, K. Yang, S.-Z. Huang, X. Li, G. Zhang, L. Bai, X.-P. Shao, Deeply seeing through highly turbid water by active polarization imaging. *Opt. Lett.* 43, 4903-4906 (2018).
30. M. Born, E. Wolf, Principles of optics: Electromagnetic theory of propagation, interference and diffraction of light. (Cambridge: Cambridge University Press, 1999).
31. N.-A. Rubin, G. D'Aversa, P. Chevalier, Z.-J. Shi, W.-T. Chen, F. Capasso, Matrix Fourier optics enables a compact full-stokes polarization camera. *Science* 365, 1-8 (2019).
32. J. Scholler, Motion artifact removal and signal enhancement to achieve in vivo dynamic full field OCT. *Opt. Express* 14, 19562-19572 (2019).
33. S. Jeong, Y.-R. Lee, W. Choi, S. Kang, J.-H. Hong, J.-S. Park, Y.-S. Lim, H.-G. Park, W. Choi, Focusing of light energy inside a scattering medium by controlling the time-gated multiple light scattering. *Nat. Photonics* 12, 277-283 (2018).
34. P. Réfrégier, Mutual information-based degrees of coherence of partially polarized light with gaussian fluctuations. *Opt. Lett.* 23, 3117-3119 (2005).
35. T. Treibitz, Y.-Y. Schechner, Active polarization descattering. *IEEE Trans. Pattern Anal. Mach. Intell.* 31, 385-399 (2008).
36. S.-K. Nayar, K. Ikeuchi, T. Kanade, Determining shape and reflectance of hybrid surfaces by photometric sampling. *IEEE T. Robot.* 6, 418-431 (1990).
37. R. Basri, D.-W. Jacobs, Lambertian reflectance and linear subspaces. *IEEE Trans. Pattern Anal. Mach. Intell.* 25, 218-233 (2003).

ACKNOWLEDGEMENTS

Funding: This work is primarily supported by the National Natural Science Foundation of China (NSFC) (61705175, 62075175, 62005203); China Postdoctoral Science Foundation (2017M613063); Fundamental Research Funds for the Central Universities (XJS190502, XJS200505).

AUTHOR CONTRIBUTIONS

F. L., Y.-D. C. and R.-G. L. conceived the methods, developed the experimental setup; P.-L. H., X. L. and F. L. designed the reconstruction algorithm; M.-Y. Y. and F. L., performed and data acquisition. F. L., Y.-D. C., P.-L. H., R.-G. L., and X.-P. S. analyzed the results; F. L., P.-L. H., M.-Y. Y. and R.-G. L. contributed to write the manuscript.

COMPETING INTERESTS

The authors declare that they have no conflict of interest.

Figures

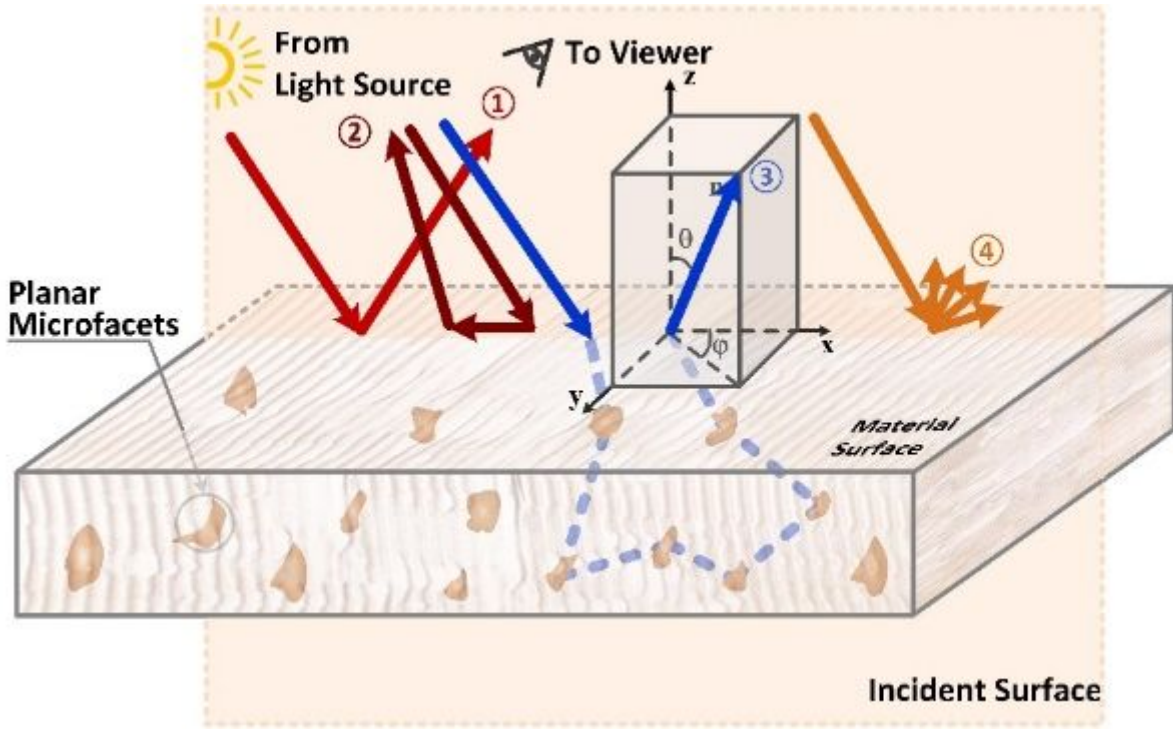


Figure 1

Reflection of light from a material surface \square specular reflection; \square - \square diffuse reflection; and \square diffraction. Most objects reflect light in both specular and diffuse patterns at the same time.

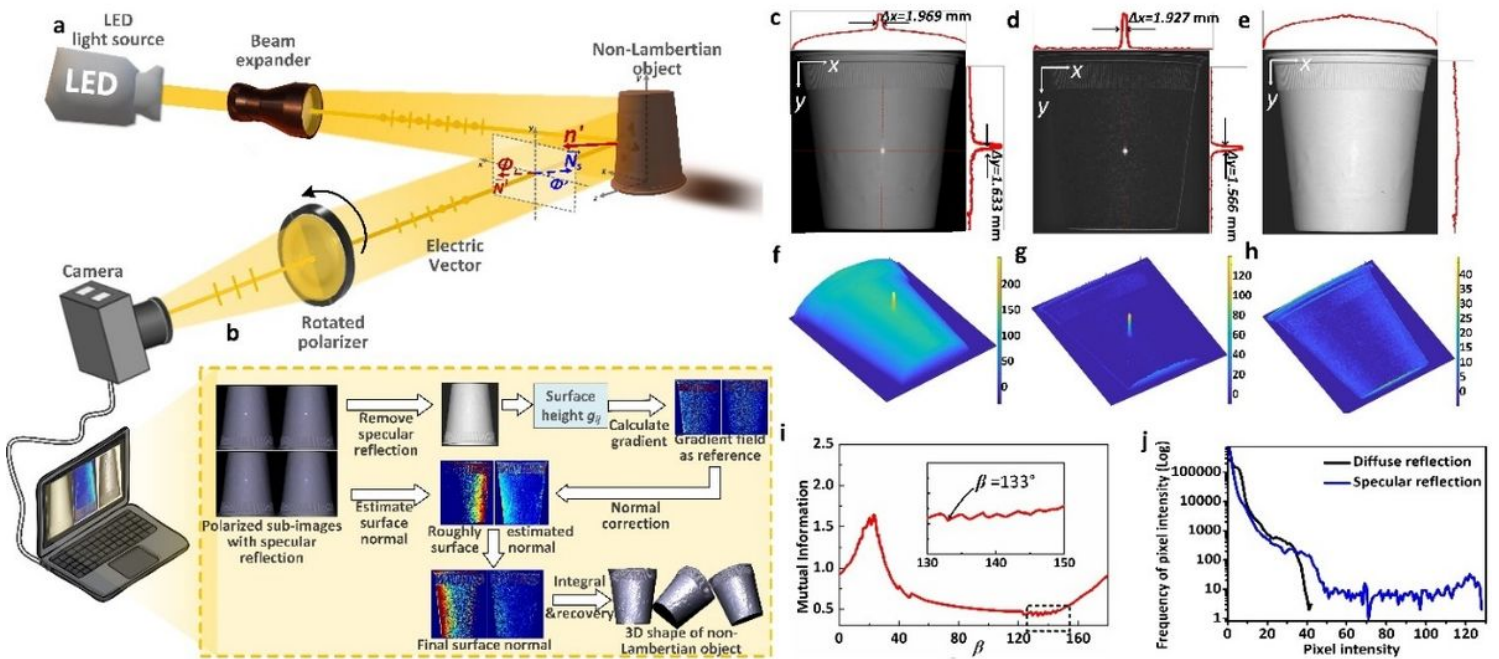


Figure 2

Overall schematic workflow. a) Polarization detection process. The light source provides unpolarized illumination in indoor experiments, and it's not necessary in outdoor conditions. Polarization information from the reflected light can be obtained with a camera and a rotated linear polarizer mounted in front of it or a camera with a pixelated polarizer. b) Mixed reflection separation and 3D information interpretation. c) raw intensity image of a foam cup with diffuse and specular reflection. d) separated specular reflection. e) Separated diffuse reflection. f), g) and h) 3D display of intensity image of c), d) and e). i) Mutual information of the estimated diffuse and specular reflection. The coefficient β can be determined by locating the lowest value to enable diffuse and specular reflection separation described in "Methods". j) The frequency of the pixel intensity of diffuse and specular reflection. Only specular reflection reaches intensity over 40, corresponding to the bright area in Fig.2(c). Both specular and diffuse reflection distribute mainly over range data below 40, demonstrating that the surface is generally covered by mixed reflection.

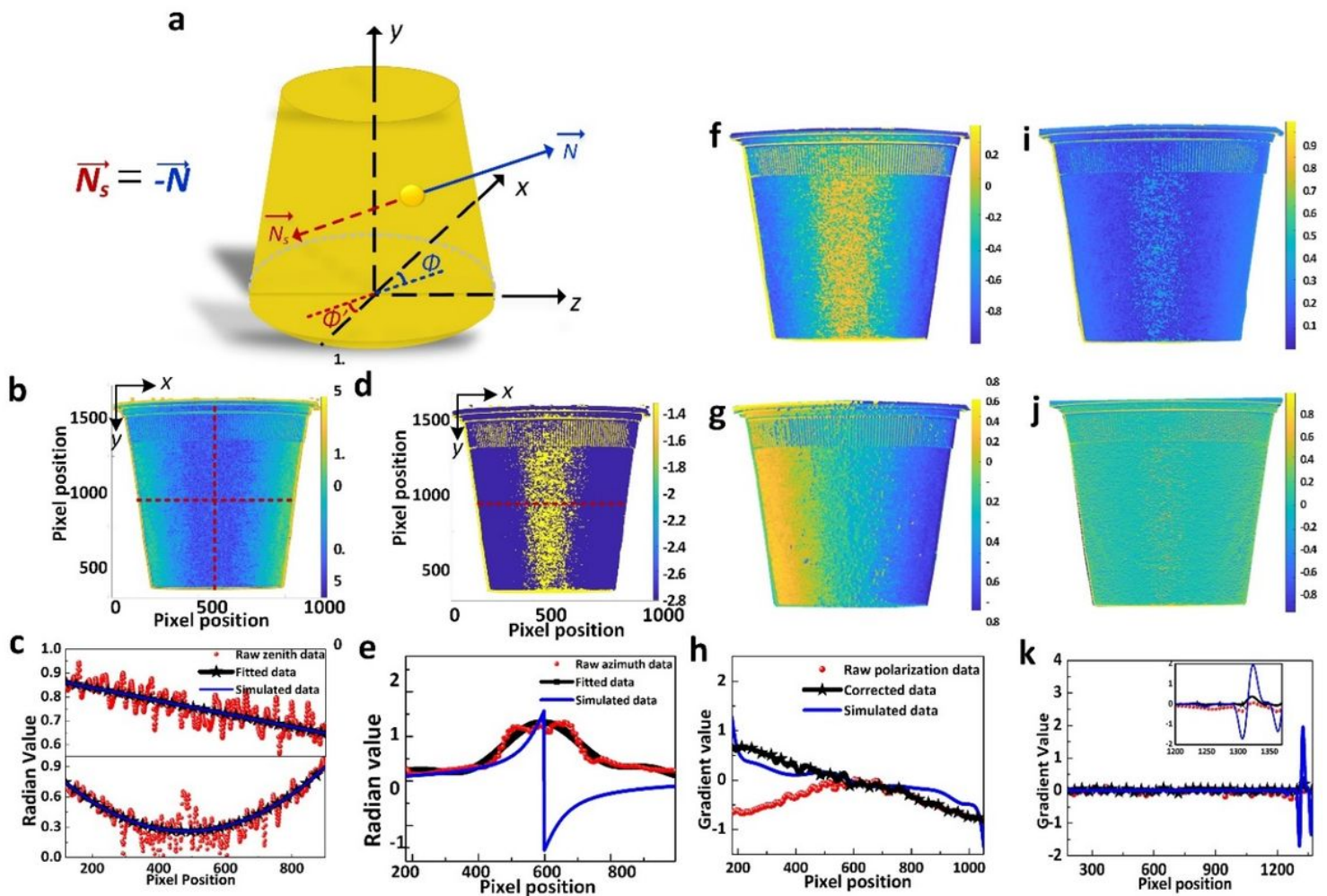


Figure 3

Surface normal correction. a) Display of surface normal ambiguity. For one point, , the estimated normal can be or , which are in opposite directions. b) and d) raw zenith and azimuth data derived from polarization. c raw and fitted zenith keep the same trend with the ideal simulated data, and e) raw and fitted azimuth in comparison with the ideal simulated data where inversion occurs around pixel 600. f) and g) 3D display of intensity image of c) and d) and e). i) Mutual information of the estimated diffuse and specular reflection. The coefficient β can be determined by locating the lowest value to enable diffuse and specular reflection separation described in "Methods". j) The frequency of the pixel intensity of diffuse and specular reflection. Only specular reflection reaches intensity over 40, corresponding to the bright area in Fig.2(c). Both specular and diffuse reflection distribute mainly over range data below 40, demonstrating that the surface is generally covered by mixed reflection.

Gpolar{grad(x)}, g) Gcor{grad(x)}, i) Gpolar{grad(y)}; j) Gcor{grad(y)}. h) Intensity variations of pixels in Row 700 of f) and g) in comparison with the simulated data, data before 600 requires correction in x direction. k) intensity variations of pixels in Column 650 of i) and j) in comparison with the simulated data, no correction is required in y direction.

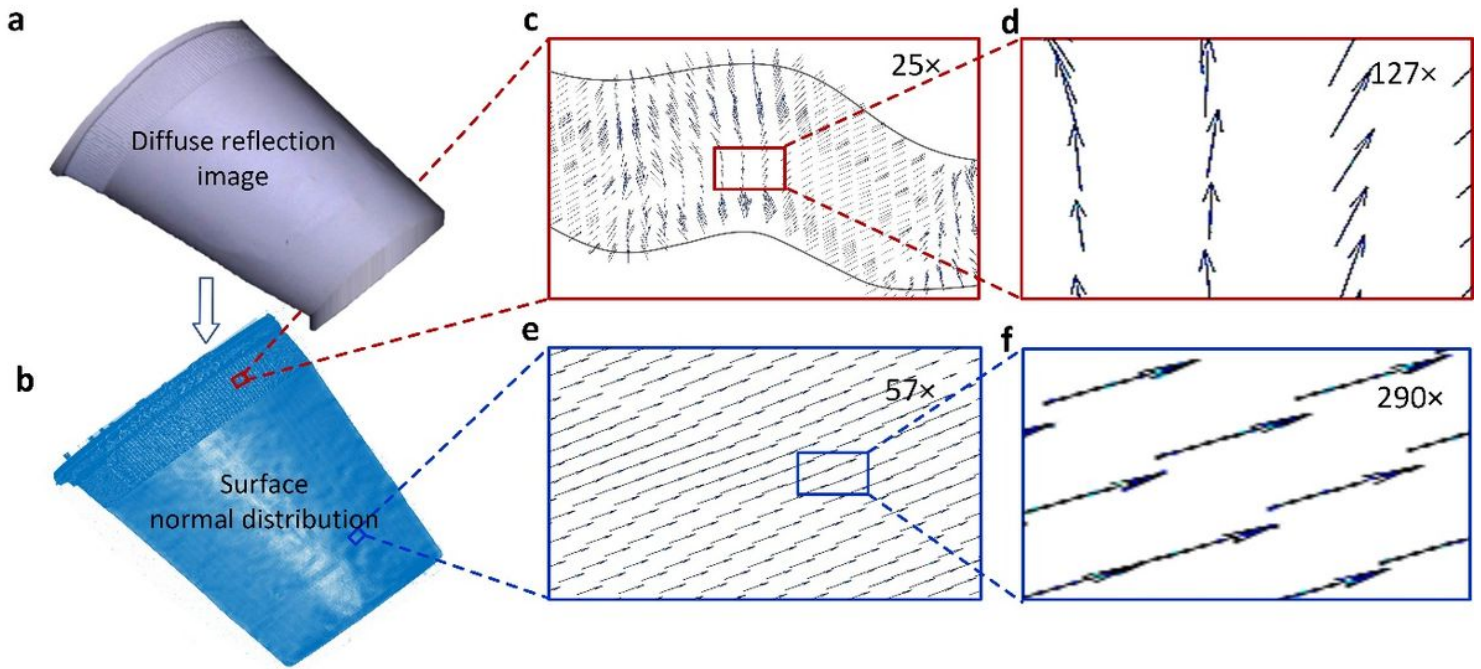


Figure 4

Normal field after correction. a) Overall surface normal display, b) and c) 25 times and 127 times magnification of the normals in the region with grooves, d) and e) 25 times and 127 times magnification of the normals in the body. The subtle difference in the directions of the normals are clearly indicated in c) and d), which is crucial to recover the accurate shape.

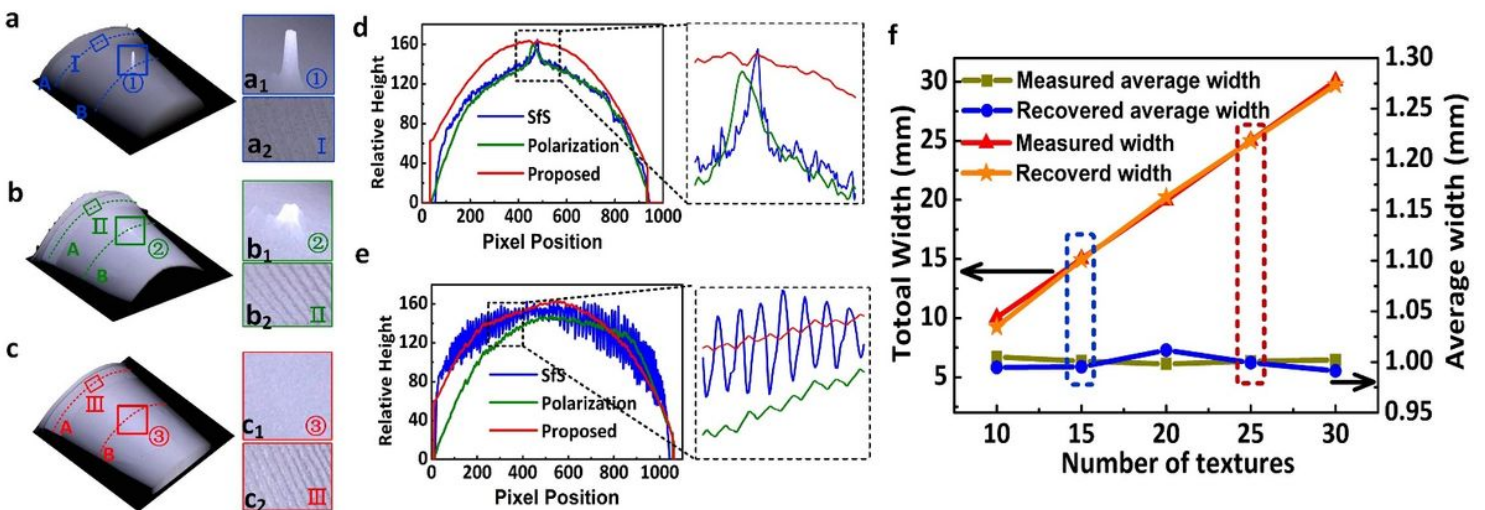


Figure 5

Recovered surface shape of the foam cup. a) Shape from shading. b) traditional shape from polarization, and c) the proposed method. Zoom-ins of the ROIs \square , \square and \square are shown in a1, b1 and c1, I, II and III are shown in a2, b2 and c2. d) contours of line A and e) contours of line B compare the performance of three different methods. f) accuracy comparison between the recovered and measured surface groove.

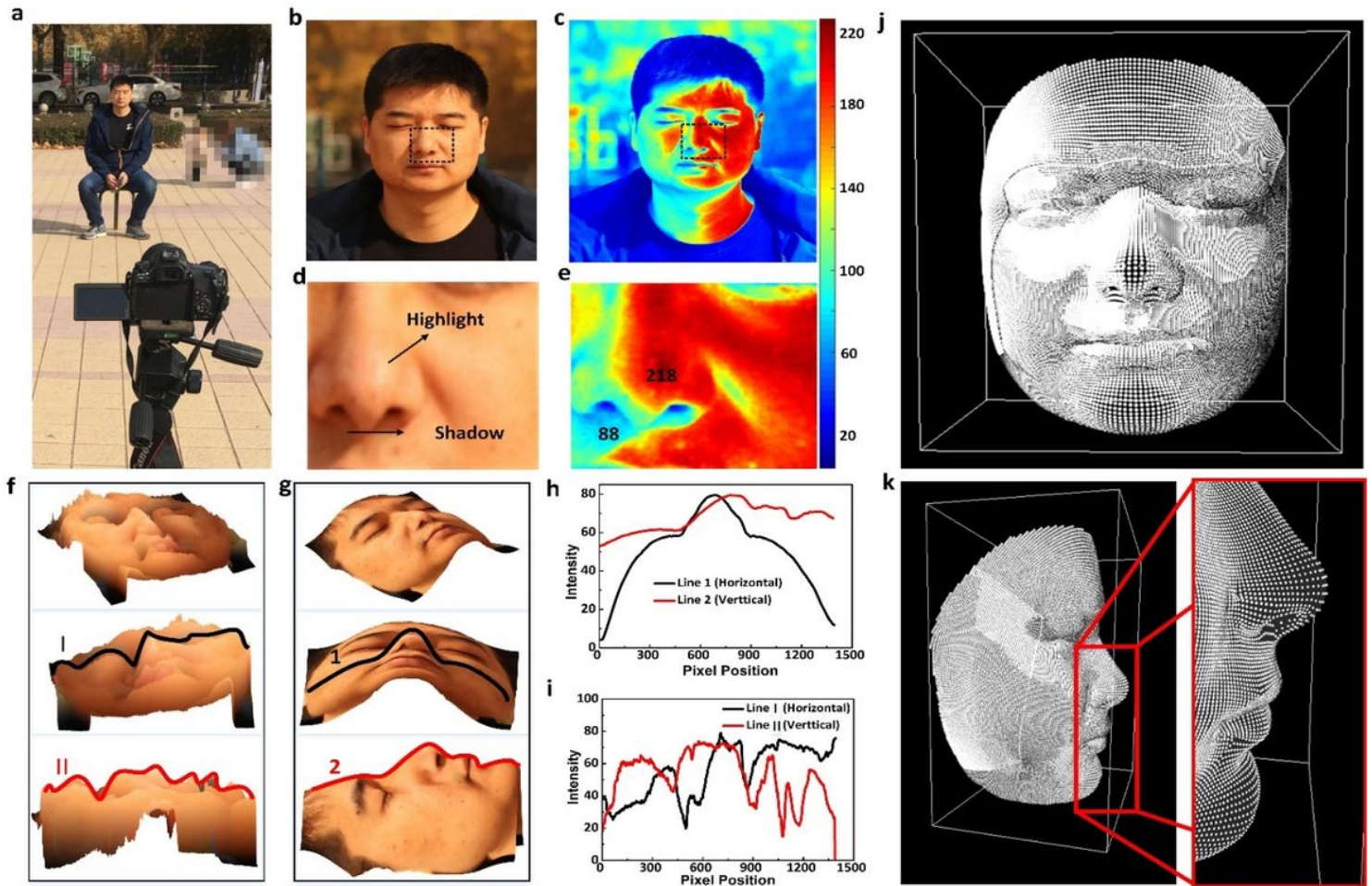


Figure 6

3D imaging of human -face in natural conditions. a) Experiment setup and condition. b) captured human face, and c) intensity distribution. d) and e) zoomed-in highlighted area and intensity distribution. f) and g) three different views of recovered 3D human face by shape from shading and proposed method. h) and i) two contours of recovered face from f) and g). j) and k) cloud data of the recovered human face by the proposed method.

Supplementary Files

This is a list of supplementary files associated with this preprint. Click to download.

- [Supplementary1XXXCupNormal.gif](#)
- [Supplementary2XXXManface.gif](#)